

The abundance of iron-peak elements and the dust composition in η Carinae: manganese

M. A. Bautista,¹^{*} M. Meléndez,^{2,3} H. Hartman,⁴ T. R. Gull⁵ and K. Lodders⁶

¹Department of Physics, Western Michigan University, Kalamazoo, MI 49008, USA

²Code 660, NASA Goddard Space Flight Center, Greenbelt, MD 20771, USA

³Department of Physics and Astronomy, Johns Hopkins University, Baltimore, MD 21218, USA

⁴Lund Observatory, Lund University, Box 43, SE-221 00 Lund, Sweden

⁵Code 667, NASA Goddard Space Flight Center, Greenbelt, MD 20771, USA

⁶Planetary Chemistry Laboratory, Department of Earth and Planetary Sciences and McDonnell Center for the Space Sciences, Washington University, Saint Louis, MO 63130, USA

Accepted 2010 September 3. Received 2010 September 1; in original form 2010 June 22

ABSTRACT

We study the chemical abundances of the *strontium filament* found in the ejecta of η Carinae. In particular, we derive the abundances of iron-peak elements from the spectra of their singly ionized ions present in the optical/infrared (IR) spectra. In this paper we analyse the spectrum of Mn II using a new non-local thermodynamic equilibrium (non-LTE) model for this system. In constructing this models we carried out theoretical calculations of radiative transition rates and electron impact excitation rate coefficients. We find that relative to Ni the gas-phase abundance ratio of Mn is roughly solar, similar to the Cr abundance but in contrast to the large enhancements in the abundances of Sc and Ti. We interpret this result as an indication of non-equilibrium condensation in the ejecta of η Carinae.

Key words: atomic data – atomic processes – line: formation – stars: abundances – stars: individual: η Carinae – ISM: atoms.

1 INTRODUCTION

η Carinae is the best known example of a nearby, massive ($>100 M_{\odot}$) stellar system approaching the end of its hydrogen-burning phase. The system currently exhibits characteristics of a luminous blue variable (LBV; Davidson & Humphreys 1997), but the 5.54-yr period discovered by Damineli (1996) and subsequent observations demonstrate the system is additionally a massive binary. During the 1840s η Carinae went through the Great Eruption ejecting a massive amount of material which today we see as the Homunculus, a neutral bipolar shell structure with intervening skirt. Lower limits to the total ejected mass, based on the normal interstellar gas to dust mass ratio are $12 M_{\odot}$, from near-infrared (near-IR) H_2 observations (Smith et al. 2006), and $40 M_{\odot}$ from APEX sub-millimeter measurements of the dust content (Gomez et al. 2010). A lesser event in the 1890s produced the Little Homunculus, a $0.5 M_{\odot}$, ionized bipolar structure also with skirt located internal, and aligned, to the Homunculus (Ishibashi et al. 2003). Ionized structures external to the Homunculus show strong nitrogen and helium enhancement with virtually no carbon or oxygen (Davidson et al. 1986). Internal to the Homunculus, within tenths of an arcsec (a few hundred au) of η Carinae are the partially ionized Weigelt

blobs whose spectra are consistent with 100-fold depletion of carbon and oxygen relative to solar abundances (Verner et al. 2002, 2005). The major depletions of carbon and oxygen with excess of nitrogen are consistent with ejecta originating from an individual massive star at the end of its hydrogen-burning phase, provided that the initial stellar mass was over $60 M_{\odot}$ (Meynet & Maeder 2002).

Hillier et al. (2001, 2006) modelled the wind of the primary, η Car A, confirming the large underabundances of carbon and oxygen and overabundance of nitrogen. While the models could not clearly determine the abundance of helium relative to hydrogen, enhancements of helium as much as 10-fold due to hydrogen burning were consistent with the observed stellar spectrum.

A peculiar, partially ionized structure, known as the strontium filament, is located about 1.5 arcsec to the northeast of η Carinae moving at -100 km s^{-1} . Position and velocity shows it lies in the plane defined by the Homunculus skirt, having originated from the two major ejections. The name refers to the original discovery by identification of two [Sr II] emission lines lying to the red of $H\alpha$ (Zethson et al. 2001). No hydrogen or helium emission lines are present at this position and velocity. Only weak [C I] emission is identified among the light elements, but hundreds of emission lines from iron-peak elements are present between 2500 and $10\,400 \text{ \AA}$, including Ca II, Sc II, Ti II, V II, Cr II, Fe II and Ni II. In their survey atlas, Hartman et al. (2004) identified more than 200 lines of Ti II, the dominant ionic species. Interestingly, the spectrum of

*E-mail: manuel.bautista@wmich.edu

the filament, unlike that of the Weigelt blobs, shows no evidence for fluorescence from Ly α radiation. Instead, the spectrum seems to result from a cool, extended ionization front, where elements with ionization potential lower than Fe (7.9 eV) are photoionized but the ionization front is devoid of higher energy photons, particularly Lyman-continuum photons, through attenuation by intervening gas at the boundary of an H II region supported by the hotter, smaller companion, η Car B, thought to be a massive O or WR star (Verner et al. 2002, 2005). Thus, the strontium filament, rich in metallic emission lines not normally seen in H II regions or neutral interstellar clouds, arguably is the best location in the nebula to study the chemical abundances of η Carinae from emission-line spectroscopy.

We engaged in a systematic study of the physical conditions in the filament responsible for the observed spectrum as well as the determination of chemical abundances of the plasma. As there was very limited spectroscopic information on the ionic species of interest, we needed to compute the atomic parameters and construct spectral models for each of the iron-peak species identified in the spectrum. In Bautista et al. (2002) we investigated the origin of the Sr II emission in the filament and deduced for this region an electron density of $n_e \approx 10^7 \text{ cm}^{-3}$ and a continuum radiation flux that can be approximated by a 35 000 K blackbody diluted by a factor $w \approx 10^{-10}$. Later, in Bautista et al. (2006) we analysed the [Ni II] and [Ti II] emission from the strontium filament and confirmed the previous diagnostics. In addition, we constrained the electron temperature of the gas to $7000 \pm 1000 \text{ K}$. Surprisingly, this study yields a Ti/Ni gas abundance ratio that is ~ 40 times the solar value. In a later paper of the series (Bautista et al. 2009) we studied the spectra of Sc II and Cr II. These ions provided consistency with previous diagnostics but yielded abnormal relative abundances. The Sc/Ni abundance ratio in gas in the filament is about 40 times the solar ratio, while the Cr/Ni ratio is roughly solar. It was concluded that such abnormal gas-phase abundances were the results of selective destruction of grains containing highly refractory elements or of non-equilibrium dust formation.

In this paper we continue our study of the spectrum of the strontium filament observed with the Space Telescope Imaging Spectrograph (STIS) instrument onboard of the *Hubble Space Telescope* (HST). This time, we analyse the emission spectrum of Mn II. To do that, first we calculate radiative transition rates and electron-impact collision strengths for these species using ‘state-of-the-art’ atomic physics methods. Then, we calculate the gas-phase abundance of Mn in the observed region.

2 OBSERVED LINE INTENSITIES

The spectra used in the present work were observed with the STIS onboard the HST during 2001 November. The $52 \times 0.2 \text{ arcsec}^2$ aperture was oriented almost along the axis of the Homunculus at a position angle of -130° . These spectra are described in more detail in Hartman et al. (2004). We extracted a 0.25 arcsec long portion of the spectrum at the peak of the strontium filament located at a projected angular distance of 2 arcsec from the star, the same region analysed in previous studies on Sr II, Ti II and Ni II (Bautista et al. 2002, 2006, 2009).

Complete spectral coverage, from the near-ultraviolet (near-UV) (2000 Å) through near-red (10 400 Å), was broken up during several HST visits of η Carinae. Hence the long-slit observations were done at several position angles, determined by HST spacecraft constraints at the time of observation. Each observation overlapped on the same spatial segment of the strontium filament. We learned substantially

more about the spatial/velocity structure in line of sight using spectra recorded at identical grating settings, but at different position angles. We identified the stronger velocity component, -100 km s^{-1} , seen uniquely in the Sr II and Ti II lines. Other, but not all, elements have an additional, but weaker, component at -160 km s^{-1} . In this and previous papers we chose to analyse only the -100 km s^{-1} component as it is common to all elements and thereby we could obtain abundance ratios. In the 2001 November data, \hat{E} lines having several velocity components were fitted by two Gaussians with centre velocities fixed at -100 and -160 km s^{-1} , respectively. As these lines are marginally resolved, our flux measures for each component are naturally less certain than for the single-component lines. The Mn II lines were fitted with two components, allowing us to derive the contribution from the -100 km s^{-1} component. The Sc II lines are weaker, but the velocities of the lines are consistent with a single component at -100 km s^{-1} .

The complete list of lines used for the present study and their measured intensities, uncorrected for extinction, are given in Table 1.

3 ATOMIC DATA AND MODELS FOR MN II

3.1 Radiative data for Mn II

We calculated radiative transition rates for dipole allowed and forbidden transitions of Mn II using the atomic structure code AUTOSTRUCTURE (Badnell 1986). This method uses the Thomas–Fermi–Dirac–Amaldi model potential (Eissner & Nussbaumer 1969) to obtain one-electron orbitals for the system. Then, wavefunctions for the atom are written as a configuration interaction expansion of the type

$$\psi_i = \sum_j c_{ji} \phi_j, \quad (1)$$

where the coefficients c_{ji} are chosen so as to diagonalize $\langle \psi_j | H | \psi_i \rangle$, where H is the Hamiltonian and the basic functions ϕ_j . The configurations included in our expansion of the Mn II system and the scaling parameters used in the potential are listed in Table 2.

For the calculation of oscillator strengths and transition rates (f - and A -values) the ion model was improved by the use of semi-empirical corrections in the form of term energy corrections (TECs). TECs introduce significant effects of the relativistic wavefunction, ψ_i^r , through perturbation expansion of the non-relativistic function ψ_i^{nr} ,

$$\psi_i^r = \psi_i^{\text{nr}} + \sum_{j \neq i} \psi_j^{\text{nr}} \frac{\langle \psi_j^{\text{nr}} | H_{1b} + H_{2b} | \psi_i^{\text{nr}} \rangle}{E_i^{\text{nr}} - E_j^{\text{nr}}}, \quad (2)$$

a modified H_{nr} is constructed with improved estimates of the differences $E_i^{\text{nr}} - E_j^{\text{nr}}$ so as to adjust the centres of gravity of the spectroscopic terms to the experimental values. The calculated term energies with and without TECs are compared in Table 3 with experimental energies, as compiled by National Institute of Standards and Technology (NIST) (Ralchenko et al. 2008).

A consistency check on the accuracy of the wavefunctions can be obtained by comparing computed gf -values in the length and velocity gauges of the dipole operator. Such comparison is presented in Fig. 1 for all dipole allowed transitions of Mn II considered in our model. The two forms of the gf -values are consistent with each other. However, the values in the length gauge tend to be systematically greater than those in the velocity gauge. None the

Table 1. Mn II lines observed in the STIS spectra of the strontium filament of η Carinae on 2001 November. Intensities, uncorrected for extinction, are in units of 10^{-14} erg s $^{-1}$ cm $^{-2}$ arcsec $^{-1}$.

Wavelength (Å)	Velocity (km s $^{-1}$)	Multiplet	Intensity	Transition
3442.974	−124	(3)	78.6	3d 5 4p z 5 P $_3^o$ – 3d 6 5 D $_4$
3461.307	−116	(3)	64.2	3d 5 4p z 5 P $_2^o$ – 3d 6 5 D $_3$
3475.035	−107	(3)	73.7	3d 5 4p z 5 P $_3^o$ – 3d 6 5 D $_3$
3483.902	−117	(3)	60.4	3d 5 4p z 5 P $_2^o$ – 3d 6 5 P $_2$
3483.902	−110	(3)	44.7	3d 5 4p z 5 P $_1^o$ – 3d 6 5 P $_1$
3489.765	−94	(3)	30.8	3d 5 4p z 5 P $_1^o$ – 3d 6 5 P $_0$
3496.833	−72	(3)	35.0	3d 5 4p z 5 P $_3^o$ – 3d 6 5 P $_2$
5395.713	−90	(9F)	6.32	3d 5 4s b 5 D $_2$ – 3d 6 a 5 D $_4$
5474.872	−106	(9F)	8.15	3d 5 4s b 5 D $_2$ – 3d 6 a 5 D $_3$
5496.302	−114	(9F)	7.05	3d 5 4s b 5 D $_4$ – 3d 6 a 5 D $_3$
6412.900	−107	(8F)	6.32	3d 5 4s b 5 P $_2$ – 3d 6 a 5 D $_4$
6425.224	−101	(8F)	7.46	3d 5 4s a 5 P $_3$ – 3d 6 a 5 D $_4$
6511.434	−112	(8F)	7.60	3d 5 4s a 5 P $_1$ – 3d 6 a 5 D $_3$
6537.786	−104	(8F)	6.24	3d 5 4s a 5 P $_3$ – 3d 6 a 5 D $_3$
6658.570	−104	(8F)	1.64	3d 5 4s a 5 P $_2$ – 3d 6 a 5 D $_1$
6852.215	−114	(2F)	1.01	3d 6 a 5 D $_4$ – 3d 5 4s a 7 S $_3$
6980.380	−105	(2F)	1.52	3d 6 a 5 D $_3$ – 3d 5 4s a 7 S $_3$
7563.501	−115	(7F)	40.1	3d 5 4s a 5 G $_6$ – 3d 6 a 5 D $_4$
7705.686	−114	(7F)	12.7	3d 5 4s a 5 G $_5$ – 3d 6 a 5 D $_3$
7807.566	−99	(7F)	7.14	3d 5 4s a 5 G $_2$ – 3d 6 a 5 D $_2$
7811.048	−103	(7F)	6.01	3d 5 4s a 5 G $_4$ – 3d 6 a 5 D $_2$
7881.401	−102	(7F)	8.73	3d 5 4s a 5 G $_2$ – 3d 6 a 5 D $_1$

Table 2. Configuration expansions for Mn II and scaling parameters λ_{nl} for each orbital in the Thomas–Fermi–Dirac potential with a core configuration equal to $1s^2 2s^2 2p^6$.

Configurations
Spectroscopic configurations:
3s 2 3p 6 3d 5 4s, 3s 2 3p 6 3d 6 , 3s 2 3p 6 3d 5 4p
3s 2 3p 6 3d 4 4s 2 , 3s 2 3p 6 3d 4 4s4p
Correlation configurations:
3s 2 3p 6 3d 5 4d, 3s 2 3p 6 3d 5 4f, 3s 2 3p 6 3d 5 5s
3s 2 3p 6 3d 5 5p, 3s 2 3p 6 3d 5 5d, 3s 2 3p 6 3d 5 6s
3s 2 3p 6 3d 5 6d
3s 2 3p 5 3d 5 4s 2 , 3s 2 3p 4 3d 6 4s 2 , 3s 2 3p 3 3d 7 4s 2
3s 2 3p 5 3d 6 4s, 3s 2 3p 5 3d 6 4p, 3s 2 3p 5 3d 6 4d
3s 1 3p 6 3d 6 4s, 3s 1 3p 6 3d 6 4p, 3s 1 3p 4 3d 7 4s 2
3s 1 3p 5 3d 6 4s 2 , 3s 1 3p 6 3d 5 4s 2 , 3s 1 3p 5 3d 7 4s
3s 1 3p 5 3d 7 4p, 3p 6 3d 6 4s 2 , 3p 5 3d 7 4s 2
3p 6 3d 7 4s, 3p 6 3d 7 4p
λ_{nl}
1s: 1.431 90, 2s: 1.131 90, 2p: 1.074 80, 3s: 1.091 50,
3p: 1.071 70, 3d: 1.076 30, 4s: 1.072 00, 4p: 1.038 70,
4d: 1.480 70, 4f: 1.067 50, 5s: 1.605 00, 5p: 1.011 70,
5d: −0.741 60, 6s: −0.800 70, 6d: −0.741 90

less, the mean dispersion is only 0.09 dex (<24 per cent), a good indicator of the overall uncertainty of the calculated values.

Next, we compare our results with the experimental determinations of Kling et al. (2001) and previous calculations of Kurucz & Bell (1995). In Table 4 we compare our calculated values with the lifetimes of several 3d 5 4p levels measured by Kling et al. With the exception of the 3d 4 4p 5 D $_1$ level, our computed lifetimes are systematically lower than those measured by Kling et al. None the less, the average difference is only 20 per cent, with a minimum

and maximum difference of 9 and 32 per cent for the 3d 4 4p 5 D $_2$ and 3d 4 4p 5 D $_1$ levels, respectively.

Fig. 2 compares the present gf -values for dipole allowed transitions with those of Kling et al. (2001) and Kurucz & Bell (1995). The average difference between the present data and that of Kling et al. is 0.23 dex for transitions with $\log_{10}(gf) > -1$, while the average difference between Kurucz’s data and experiment is 0.21 dex for the same transitions. As expected, the discrepancies of our computed individual gf -values are worse than computed lifetimes, because the lifetimes are heavily weighted towards the strongest transitions of each level. The gf -values for the weaker transitions are usually more difficult both to measure and to compute.

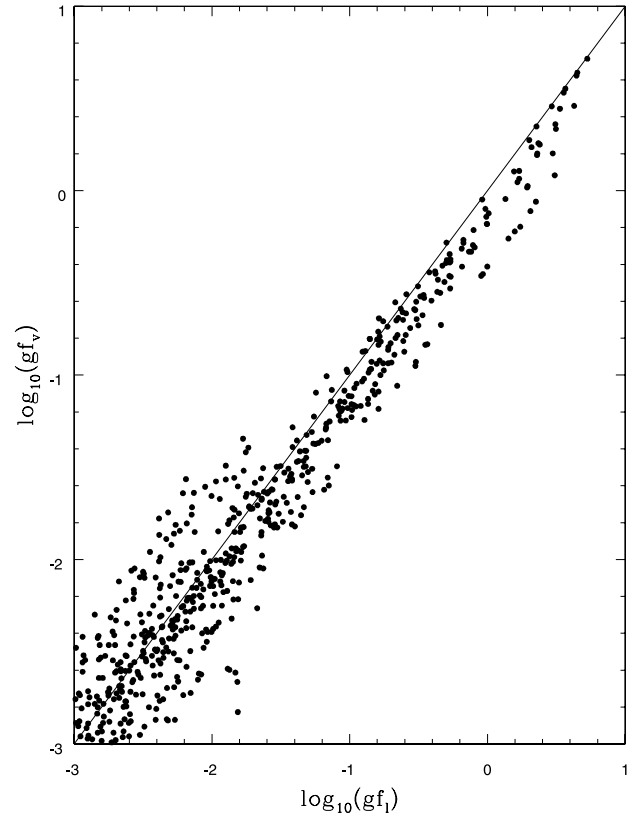
While there is good agreement between observations and calculations, we identified a few transitions that seem problematic. These transitions, listed in Table 5, are reasonably strong [$\log_{10}(gf) > -1$] but have large, unexplained differences between theoretical and experimental determinations. For the first three transitions listed in Table 5, our theoretical values agree well with the theoretical results of (Kurucz & Bell 1995). However, the tabulated values measured by (Kling et al. 2001) are nearly an order of magnitude lower. Our calculated value for the fourth transition agrees with experiment, but the value listed by Kurucz is overestimated by 1.2 dex.

Based on these comparisons, we assign overall uncertainties of 0.2 dex to the present gf -values and the radiative rates for dipole allowed transitions. However, the accuracy is systematically better for the strongest transitions that dominate the spectrum, and worse for the weaker transitions. For the remainder of this paper we adopt a data set of gf -values from (Kling et al. 2001) when available and our calculated values otherwise.

Our model ion was also used to compute electric quadrupole and magnetic dipole transition rates which to the best of our knowledge is the first time that such rates are reported.

Table 3. Term energies for Mn II (in Ryd). The table shows results computed without term energy corrections Theo.¹, with term energy corrections Theo.² and experimental energies from NIST (Ralchenko et al. 2008).

	Config.	Term	Theo. ¹	Theo. ²	Exp.
1	3d ⁵ 4s	⁷ S	0.000 000	0.000 000	0.000 0000
2	3d ⁵ 4s	⁵ S	0.089 612	0.086 314	0.086 3241
3	3d ⁶	⁵ D	0.125 512	0.133 120	0.133 1120
4	3d ⁵ 4s	⁵ G	0.310 935	0.251 274	0.251 2538
5	3d ⁶	³ P	0.309 568	0.276 385	0.276 4186
6	3d ⁵ 4s	⁵ P	0.348 486	0.272 595	0.272 5895
7	3d ⁶	³ H	0.330 193	0.279 333	0.279 3151
8	3d ⁶	³ F	0.313 795	0.288 376	0.288 1917
9	3d ⁵ 4s	⁵ D	0.348 486	0.299 207	0.299 1611
10	3d ⁵ 4s	³ G	0.373 900	0.301 126	0.302 6890
11	3d ⁶	³ G	0.330 193	0.319 300	0.317 8169
12	3d ⁵ 4s	³ P	0.409 763	0.331 059	0.331 0650
13	3d ⁶	³ D	0.381 652	0.344 184	0.344 8378
14	3d ⁵ 4p	⁷ P ^o	0.320 749	0.351 818	0.351 8282
15	3d ⁶	¹ I	0.372 748	0.352 890	0.352 8428
16	3d ⁶	¹ G	0.386 235	0.354 589	0.354 4990
17	3d ⁵ 4s	³ D	0.439 597	0.363 414	0.362 8145
18	3d ⁶	¹ S	0.420 977	0.371 567	0.371 4280
19	3d ⁵ 4s	³ I	0.457 399	0.375 368	0.375 3637
20	3d ⁶	¹ D	0.450 610	0.393 091	0.393 0420
21	3d ⁵ 4s	⁵ F	0.510 884	0.395 772	0.397 2288
22	3d ⁵ 4s	³ D	0.497 263	0.399 927	0.396 7836
23	3d ⁵ 4p	⁵ P ^o	0.374 814	0.395 956	0.395 9458
24	3d ⁵ 4s	¹ I	0.487 229	0.403 725	0.403 8295
25	3d ⁵ 4s	³ F	0.507 136	0.408 844	0.407 3692
26	3d ⁵ 4s	¹ D	0.528 895	0.528 428	0.427 4140
27	3d ⁵ 4s	¹ F	0.545 315	0.427 658	0.428 9658
28	3d ⁵ 4s	³ H	0.551 139	0.441 058	0.440 7694
29	3d ⁶	¹ F	0.491 366	0.451 025	0.449 1755
30	3d ⁵ 4s	³ G	0.560380	0.450 550	0.450 8358
31	3d ⁵ 4s	³ F	0.571057	0.454 899	0.454 4418
32	3d ⁵ 4s	¹ H	0.581 817	0.469 974	0.469 7860
33	3d ⁵ 4s	³ F	0.598 696	0.477 126	0.477 3137
34	3d ⁵ 4s	¹ G	0.585 586	0.497 212	0.479 8119
35	3d ⁶	³ P	0.537 646	0.485 250	0.485 3173
36	3d ⁶	³ F	0.541 627	0.489 701	0.489 9977
37	3d ⁵ 4s	¹ F	0.629 822	0.508 347	0.508 1159
38	3d ⁵ 4s	³ S	0.651 485	0.518 485	0.518 3595
39	3d ⁶	¹ G	0.607 930	0.525 248	0.542 5450
40	3d ⁵ 4s	³ D	0.724 466	0.570 522	0.570 2464
41	3d ⁵ 4p	⁵ G ^o	0.613 735	0.587 786	0.587 8393
42	3d ⁵ 4p	⁵ H ^o	0.626 295	0.598 631	0.598 6337
43	3d ⁵ 4p	⁵ F ^o	0.633 367	0.607 602	0.607 6835
44	3d ⁵ 4p	⁵ D ^o	0.652 280	0.610 124	0.610 2206
45	3d ⁵ 4p	⁵ S ^o	0.651 724	0.609 887	0.609 9067
46	3d ⁵ 4p	³ H ^o	0.652 482	0.618 086	0.618 0621
47	3d ⁵ 4p	³ F ^o	0.649 638	0.618 084	0.618 0500
48	3d ⁵ 4p	⁵ P ^o	0.662 737	0.622 877	0.623 0885
49	3d ⁵ 4p	³ P ^o	0.675 878	0.630 345	0.630 1199
50	3d ⁵ 4p	⁵ F ^o	0.693 008	0.641 814	0.641 8974
51	3d ⁵ 4p	³ G ^o	0.675 706	0.642 612	0.642 7287
52	3d ⁵ 4p	³ D ^o	0.696 313	0.650 460	0.645 9466
53	3d ⁵ 4p	⁵ P ^o	0.693 008	0.650 017	0.650 0995
54	3d ⁵ 4s	¹ S	0.684 912	0.684 915	
55	3d ⁵ 4p	⁵ D ^o	0.702 275	0.657 852	0.657 8936
56	3d ⁵ 4p	³ D ^o	0.718 750	0.650 460	0.668 8107
57	3d ⁵ 4p	³ F ^o	0.723 451	0.669 124	0.671 9821
58	3d ⁵ 4p	³ S ^o	0.722 247	0.673 429	0.673 5320

**Figure 1.** $\log_{10}(gf)$ values calculated in the velocity gauge against those in the length gauge for dipole allowed transitions of Mn II.

3.2 Electron impact excitation of Mn II

We have computed electron impact collision strengths for transitions among the lowest 158 energy levels of Mn II that belong to the configurations 3d⁶, 3d⁵4s and 3d⁵4p.

We employ the Breit–Pauli *R*-matrix method implemented in the BPRM set of codes developed in the framework of the IRON Project (Hummer et al. 1993; Berrington et al. 1995).

The calculations include partial wave contributions with angular momentum $L = 0$ –10. The collision strengths were ‘topped up’ with estimates of contributions from higher partial waves based on the Coulomb–Bethe approximation (Burgess 1974). Collision strengths for the fine-structure levels were obtained by algebraic recoupling of the LS reactance matrices (Hummer et al. 1993). The use of pseudo-orbitals in the calculation yields non-physical resonances in the collision strengths, which in the present case became evident through peaks at energies beyond the highest threshold in the expansion. Thus, we employed the pseudo-resonance removal method of Gorzyca et al (1995). The collision strengths were sampled by 10 000 points for impact energies from 0 to 12.24 eV. Fig. 3 shows collision strengths for dipole forbidden transitions from the ground multiplet to the first four excited states. Similarly, Fig. 4 illustrates the collision strengths from dipole allowed transitions from the ground term to the first four odd parity states.

We compute Maxwellian-averaged effective collision strengths, defined as

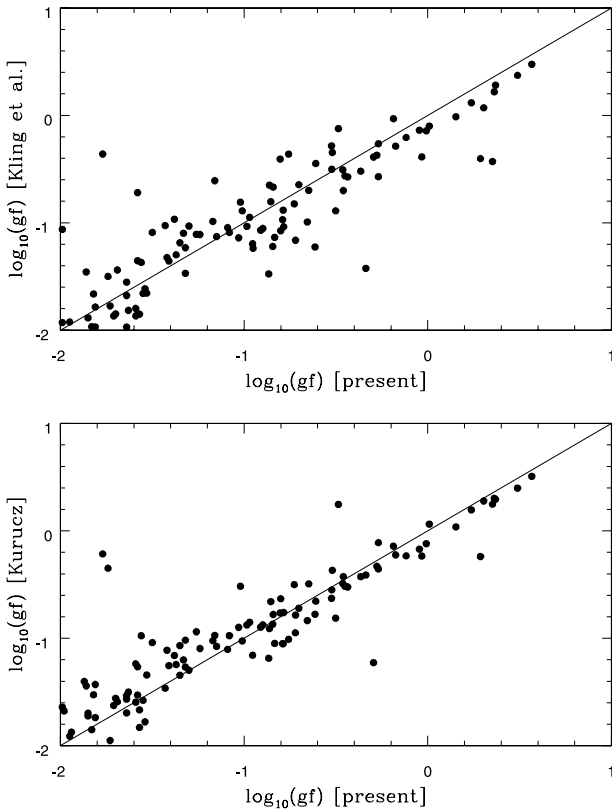
$$\Upsilon(T) = \int_0^\infty \Omega_{if}(\epsilon_f) \exp(-\epsilon_f/kT) d(\epsilon_f/kT), \quad (3)$$

Table 4. Experimental and present lifetimes of various $3d^5 4p$ levels of Mn II.

Level	Energy (cm ⁻¹)	Measurements (ns)				Present
		(a)	(b)	(c)	(d)	
$3d^5(^6S)4p\ ^7P_2$	38 366.18	3.66(5)	3.89(21)	4.4(4)	3.67(4)	2.99
$3d^5(^6S)4p\ ^7P_3$	38 543.08	3.60(5)	3.62(16)	4.4(4)	3.61(6)	2.95
$3d^5(^6S)4p\ ^7P_4$	38 806.67	3.54(5)	3.58(12)	4.7(5)	3.68(7)	2.88
$3d^5(^4G)4p\ ^5H_7$	65 846.61	—	3.93(13)	—	4.01(20)	2.89
$3d^5(^4G)4p\ ^5F_5$	66 542.53	4.0(8)	—	4.1(4)	2.66(19)	2.98
$3d^5(^4G)4p\ ^5F_4$	66 643.31	4.5(5)	—	—	2.7(3)	2.05
$3d^5(^4G)4p\ ^5F_1$	66 645.07	—	—	—	2.6(3)	2.05
$3d^5(^4G)4p\ ^5F_2$	66 676.78	—	—	—	3.2(3)	2.26
$3d^5(^4G)4p\ ^5F_3$	66 686.70	—	—	—	2.97(14)	2.19
$3d^5(^4P)4p\ ^5D_1$	66 894.09	—	—	—	2.51(15)	3.32
$3d^5(^4P)4p\ ^5D_2$	66 901.44	—	—	—	2.21(16)	2.93
$3d^5(^4P)4p\ ^5D_3$	67 009.16	—	—	—	3.55(12)	2.96
$3d^5(^4P)4p\ ^5D_4$	67 295.43	—	—	—	4.00(10)	3.25
$3d^5(^4P)4p\ ^3P_2$	69 044.90	—	—	—	3.53(20)	3.22

(a) From Pinnington et al. (1992), (b) from Schnabel, Bard & Kock (1995),

(c) from Martinson et al. (1973), (d) from Pinnington & Lutz (1974).

**Figure 2.** Comparison between experimental $\log(gf)$ values of Kling, Schnabel & Griesmann (2001) and theoretical determinations of Kurucz & Bell (1995) and our present results.

where Ω_{if} is the collision strength for the transition i to f , and ϵ_f is the energy of the outgoing electron. The Υ values were computed for various temperatures between 2000 and 30 000 K.

3.3 The multilevel model of Mn II and spectral diagnostics

We construct excitation equilibrium models for Mn II which consider electron impact excitation and continuum fluorescence excitation (see Bautista, Peng & Pradhan 1996). We assume that the

radiation field density, U_ν , at photon energies below the Lyman ionization limit (13.6 eV) can be approximated by a blackbody with temperature T_R times a geometrical dilution factor w , i.e.

$$\frac{c^3 U_\nu}{8\pi h \nu^3} = \frac{w}{\exp(h\nu/kT_R) - 1}.$$

This is a very simplified, but practical, approximation since we have no knowledge of the continuum spectrum in the direction of the filament. For the present calculations we adopt a temperature of 35 000 K as in previous calculations of Bautista et al. (2002, 2006, 2009).

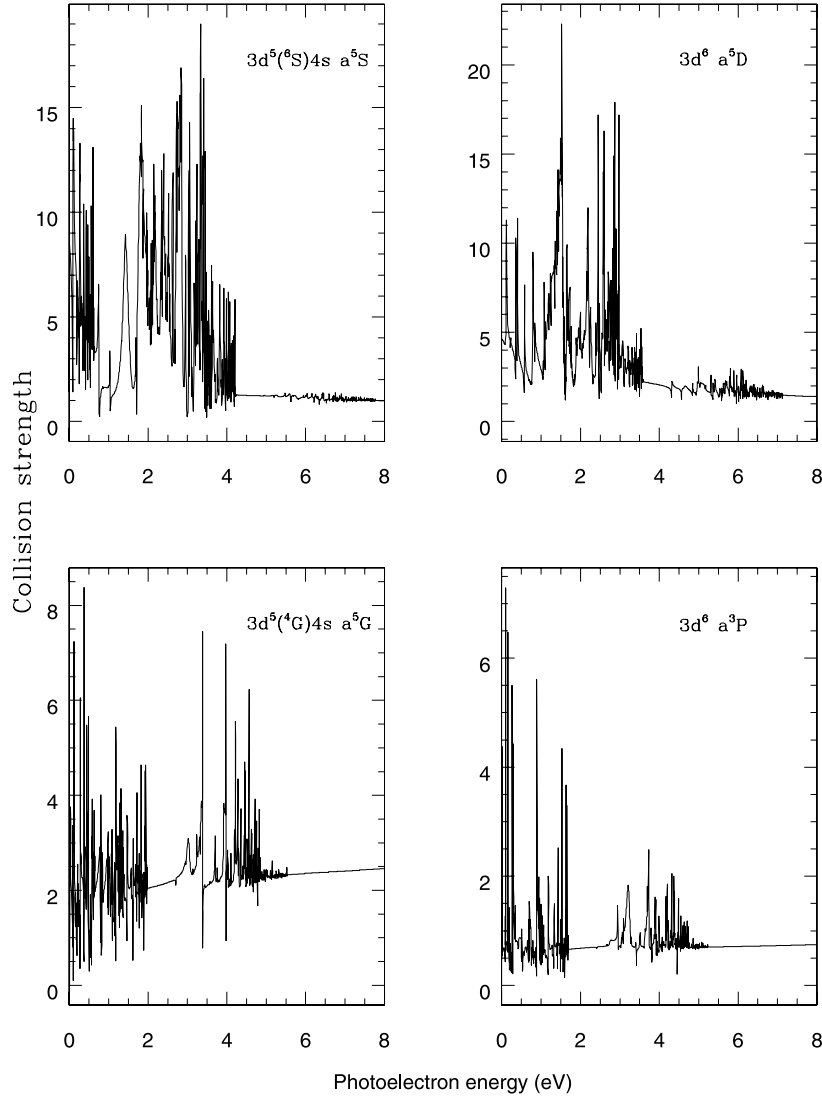
A partial Grotrian diagram for Mn II is presented in Fig. 5 showing the major lines identified in our spectra of the strontium filament. Interestingly, the spectrum shows a combination of lines excited only by electron impact excitation and of lines dominated by fluorescence. The lines excited only by electron collision originate from the a^5G state, which has no strong dipole transitions from odd parity terms pumped from the ground level. Other lines, in the visual part of the spectrum, are efficiently excited by cascades from the z^7P^o and z^5P^o states, which are pumped from the ground level. Thus, line ratios among collisional lines and lines excited by fluorescence should serve as good diagnostics for the radiation flux on the region where the spectrum is produced.

The various emissivity line ratios of Mn II are plotted against the logarithm of the dilution factor (w) in Fig. 6. The ratios, relatively insensitive to any reasonable temperature variations, are computed at the previously derived temperature of 6000 K for three different electron density 10^5 , 10^6 and 10^7 cm⁻³. The ratios are between the summed line fluxes of the 9F multiplet ($\lambda\lambda$ 5395, 5416, 5496) and the summed line fluxes of the 8F multiplet ($\lambda\lambda$ 6412, 6425, 6511, 6537, 6658) respectively relative to the summed line fluxes of the 7F multiplet ($\lambda\lambda$ 7563, 7705, 7807, 7811, 7881). By combining all the fluxes of lines from the same multiplet we diminish the observational, measurement and theoretical errors that affect ratios computed from individual lines.

As expected, these ratios are sensitive to the intensity of the continuum radiation field. A downside of these line ratios is that the wavelengths of the individual lines are relatively far apart and must be corrected for extinction before summation. Towards η Carinae and its ejecta, we have little knowledge of the extinction curve. Our best estimate of extinction affecting the strontium filament spectrum

Table 5. List of problematic dipole allowed transitions of Mn II.

Upper	Lower	Wavelength (Å)	Measured Kling et al.	$\log_{10}(gf)$ Calculated Kurucz	Calculated Present paper
$3p^5(^4G)4p^5F_4$	$3d^5(^4G)4s^5G_5$	2558.606	−0.43	0.248	0.352
$3p^5(^4G)4p^5F_4$	$3d^5(^4G)4s^5G_4$	2559.413	−1.424	−0.410	−0.337
$3p^5(^4G)4p^5D_3$	$3d^6^5D_3$	1920.014	−0.720	−1.529	−1.580
$3p^5(^4G)4p^5D_2$	$3d^6^5P_2$	2719.739	−1.500	−0.348	−1.741

**Figure 3.** LS-coupling collision strengths for dipole forbidden excitations from the ground term $3d^5 4s a^7S$ to the first four excited states of Mn II.

was reported in Bautista et al. (2006), derived from the line ratio of relatively well-known [Ni II] transitions that arise from a common upper level, i.e. $\lambda 7413(a^2D_{3/2}-a^2F_5/2)$ and $\lambda 6668(a^2D_{5/2}-a^2F_5/2)$. From those measurements and the standard interstellar extinction curve of Cardelli, Clayton & Mathis (1989) we derive as reddening $E(B - V) = 0.7 \pm 0.3$, which is equivalent to an extinction magnitude, $A_V = 2.1 \pm 0.9$ mag for a typical total-to-selective extinction of $R_V = A_V/E(B - V) = 3.1$. The relatively large uncertainty in A_V comes from the fact that the two lines used in the diagnostic are close in wavelength and in the red. This value for the extinction magnitude is consistent with the value measured, A_V

$= 2.06$ mag, from photometry of stars of the Tr 16 cluster in the Carinae nebula (Tapia et al. 2003). If there is a significant amount of circumstellar dust around η Carinae that intervenes the path from the strontium filament to the observer, the actual extinction magnitude to the filament could be somewhat higher than to the Tr 16 cluster stars. On the other hand, thermal-IR maps of the dust column density in the Homunculus reveal a local minimum near the position of the strontium filament (Smith et al. 2006), so unusual reddening in the light path may not be a serious problem. Besides the uncertainty in A_V , the actual shape of the extinction curve towards the Homunculus may be different than the normal interstellar medium

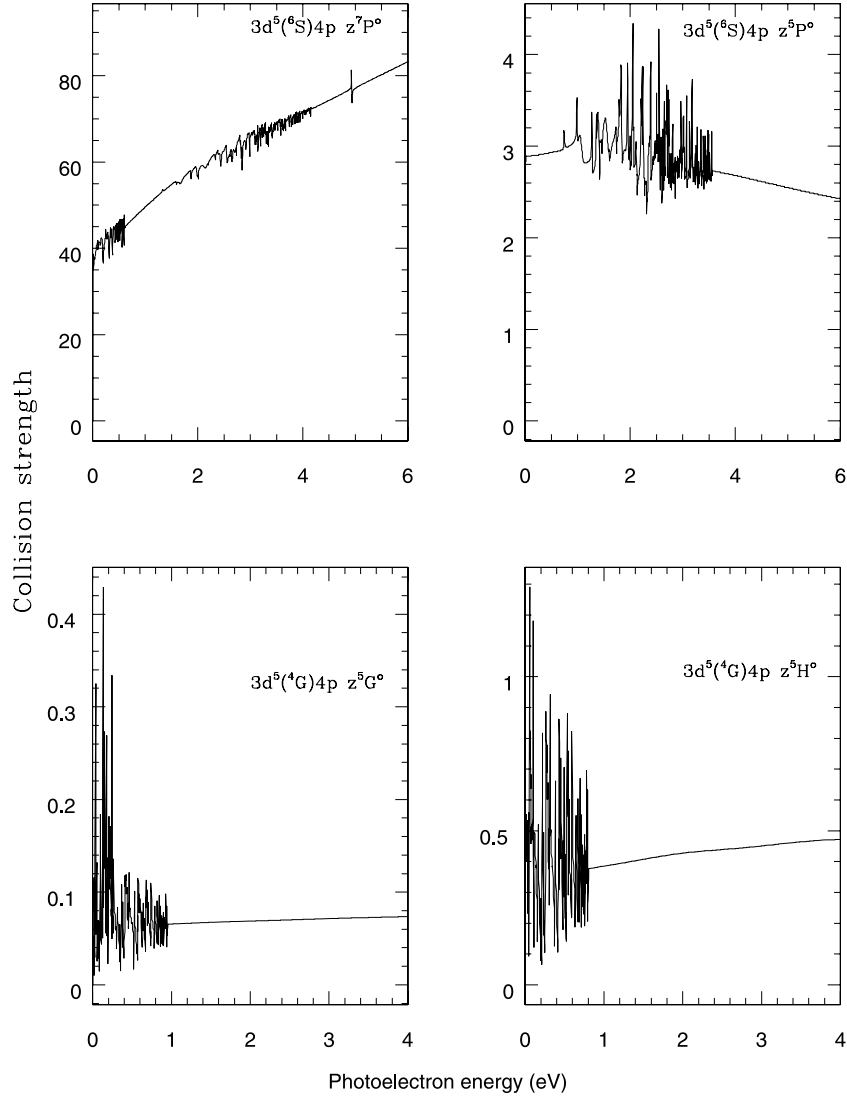


Figure 4. LS-coupling collision strengths for dipole-allowed excitations from the ground term $3d^5 4s a^7 S$ to the first four odd parity states of Mn II.

extinction. Thé & Graafland (1995) showed that R_V ranges from 3 to 5 for the O-type stars in the Carinae Nebula, with an average value around 4. Thus, Davidson & Humphreys (1997) recommended $R_V \approx 3.9$ and $A_V \approx 1.7$ mag (see also Davidson et al. 1995; Hamann et al. 1999). For the sake of simplicity through this work and in absence of a definitive determination of extinction in η Carinae we correct measured line intensities for extinction using $A_V = 2.1$ and the interstellar $R_V = 3.1$, which is good enough when comparing line fluxes of lines close in wavelength.

From Fig. 6 we conclude that the observed Mn II line ratios are consistent, within the uncertainties about extinction correction, with a dilution factor of the radiation field of $\sim 10^{-9}$. For the remainder of this paper we adopt the same physical conditions derived from previous diagnostics (Bautista 2002, 2006, 2009), i.e. $w = 10^{-9}$, $N_e = 10^7 \text{ cm}^{-3}$, $T_e = 6000 \text{ K}$.

3.4 Spectral modelling and the Mn abundance

Table 6 compares the relative intensities of [Mn II] with theoretical predictions. The comparisons are made for the measured line intensities corrected for extinction ($A_V = 2.1$, $R_V = 3.1$). Because

of the larger uncertainties in their measured fluxes and the extinction corrections, we exclude all dipole-allowed lines seen in the UV part of the spectrum. All lines here are normalized to the sum of intensities of the observed lines. The agreement between the measured and predicted [Mn II] line intensities is reasonably good.

From the present lines and those of [Ni II] from Bautista et al. (2004) we derive $N(\text{Mn II})/N(\text{Ni II}) = 0.38$ with an uncertainty conservatively estimated to be a factor of two from intrinsic uncertainties of the two spectral models, flux measurements and observed scatter between theoretical, measured and observed gf -values. This uncertainty estimate takes into account the dispersion between all the lines in the spectrum and uncertainties in the physical conditions and the atomic data.

Mn has an ionization potential of 7.43 eV, which is very similar to 7.64 eV for Ni. As Mn II and Ni II are the only ions of Mn and Ni detected in the spectrum, we suggest that $N(\text{Mn})/N(\text{Ni}) \approx N(\text{Mn II})/N(\text{Ni II}) = 0.4$. With our conservative estimate of the total uncertainty in the measured abundance ratio to be a factor of 3, this abundance ratio is in agreement with the solar ratio of $N(\text{Mn II})/N(\text{Ni II})_\odot = 0.192$ (Lodders 2003).

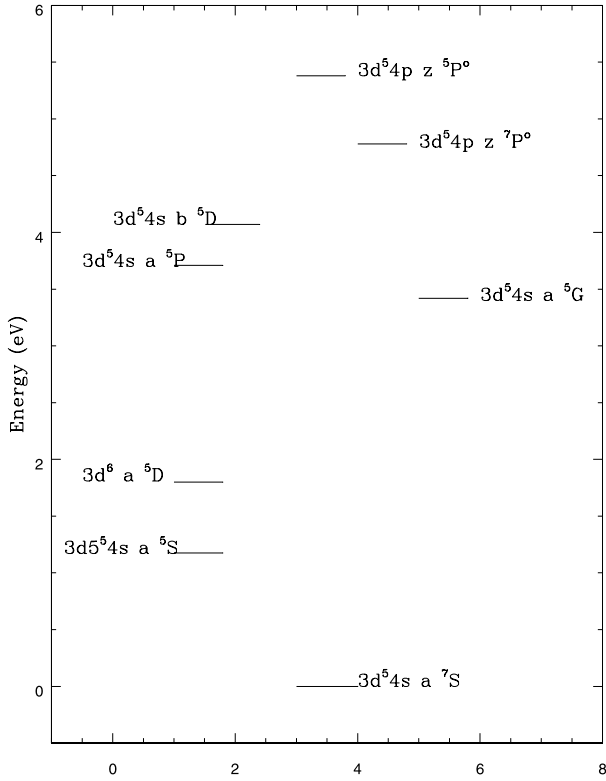


Figure 5. Partial Grotrian diagram of Mn II.

The calculated abundance ratios relative to Ni from the present determination and our previous work on other iron-peak species are plotted in Fig. 7. In Fig. 7(a), the abundance ratios are plotted against the 50 per cent condensation temperature in a CNO processed atmosphere and in Fig. 7(b), against the first ionization potential of each element. There is no clear correlation between gas-phase abundances and first ionization potential of the elements. There is a dichotomy between elements with condensation temperatures equal or lower than Ni versus elements with higher condensation temperature. The gas-phase abundances of the two elements with lower condensation temperatures than Ni agree with solar abundances, while the gas-phase abundances of the two elements with condensation temperatures hotter than Ni are greatly enhanced.

The 50 per cent condensation temperature of Mn is 919 K at 10^{-7} bar for a CNO processed gas of solar composition. Manganese is more volatile than Cr in a solar composition gas. However, the absolute 50 per cent condensation temperatures and the resulting condensates are quite different between Mn and Cr. In the CNO processed solar gas, MnSi starts to condense into a solid solution with an (Fe,Ni)Si alloy but only insignificant amounts of MnSi are in this condensate. At a lower temperature where CaS becomes stable, MnS condenses into the solid CaS, well known from meteorites (see e.g. Lodders et al. 1993, and references therein).

The observed pattern of gas-phase abundance in the strontium filament is opposite to what is expected for direct depletion of metals through chemical condensation. The observed pattern seems to require a mechanism for fractional condensation from the ejecta that obtains a spatial separation of refractory (TiC) and less refractory dust ((Fe,Ni)Si), with subsequent preferred evaporation of the more refractory dust (Bautista et al. 2006). Alternatively, condensation into dust may happen in a non-equilibrium process. If condensation was driven by Fe-shielding of photons more energetic than 7.8 eV,

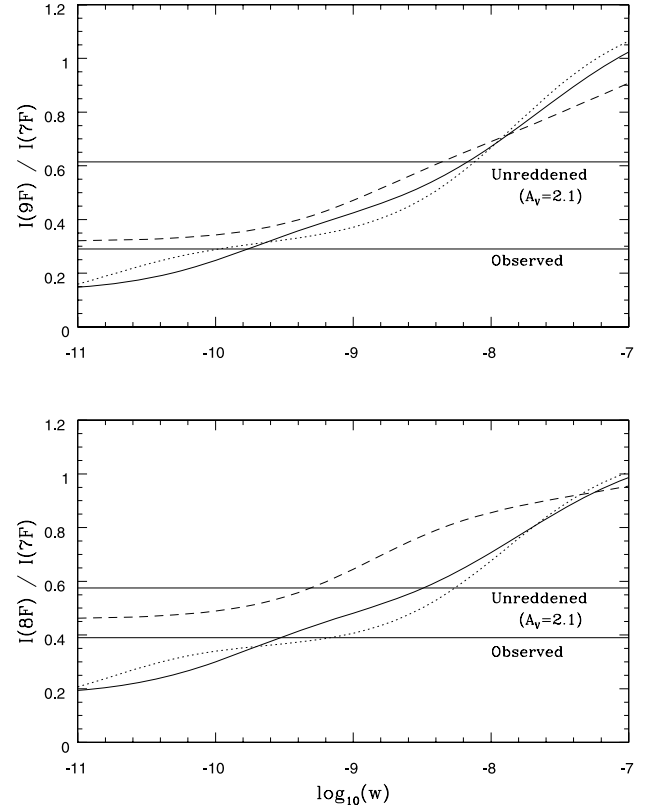


Figure 6. Mn II line emissivity line ratios against the logarithm of the dilution factor. The ratios are between the lines of the 9F multiplet ($\lambda\lambda$ 5395, 5416, 5496) and the 8F multiplet ($\lambda\lambda$ 6412, 6425, 6511, 6537, 6658) to the 7F multiplet ($\lambda\lambda$ 7563, 7705, 7807, 7811, 7881). The curves were computed for $N_e = 10^5 \text{ cm}^{-3}$ (dotted), $N_e = 10^6 \text{ cm}^{-3}$ (solid), $N_e = 10^7 \text{ cm}^{-3}$ (dashed) and $T_e = 6000 \text{ K}$. The horizontal lines indicate the measured lines ratios and the ratios corrected by extinction with $A_V = 2.1$.

Table 6. Observed and theoretical line intensities for the Mn II spectra. Line intensities are normalized relative to the total strength of all the lines observed added together. The error in the measurements is estimated in 20 per cent. The theoretical spectrum was computed for $T_e = 7000 \text{ K}$, $w = 10^{-9}$ and $N_e = 10^7 \text{ cm}^{-3}$.

λ (Å)	$I(\lambda)/\sum_i I(\lambda_i)$	
	Obs.	Theo.
5395.713	0.083	0.012
5474.872	0.103	0.090
5496.302	0.089	0.111
6412.900	0.057	0.067
6425.224	0.067	0.095
6511.434	0.066	0.051
6537.786	0.054	0.045
6658.570	0.014	0.020
6852.215	0.008	0.002
6980.380	0.011	0.002
7563.501	0.248	0.244
7705.686	0.075	0.136
7807.566	0.041	0.012
7811.048	0.034	0.076
7881.401	0.049	0.036

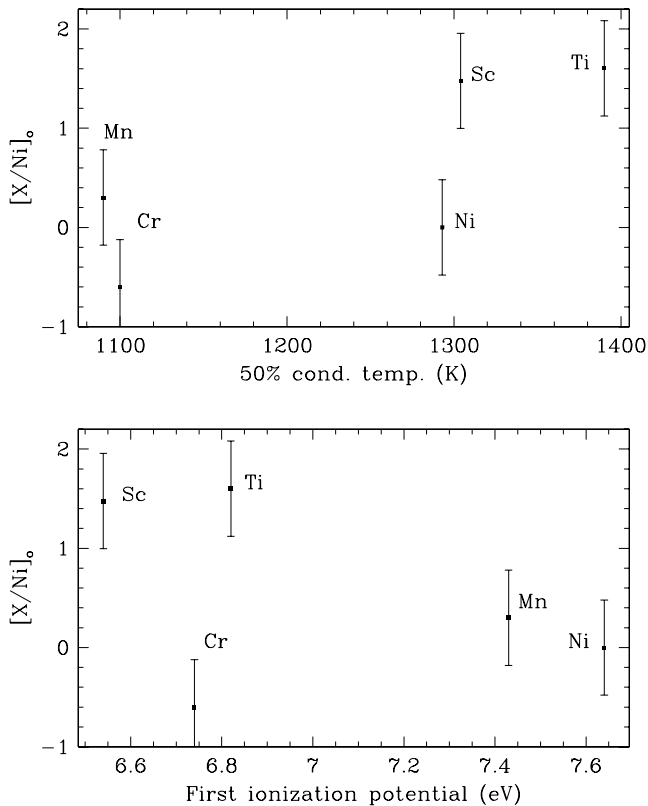


Figure 7. Chemical enhancements of iron-peak elements relative to nickel in the strontium filament of η Carinae. The abundance ratios are plotted versus the 50 per cent equilibrium condensation temperature in a CNO processed plasma and the first ionization potential of the elements.

then Sc and Ti, which have lower ionization potentials (only 6.54 and 6.82 eV, respectively), remained photoionized and, hence, could not condense efficiently. One possible problem with this scenario is that the gas-phase abundance of Cr, which also has a low first ionization potential of 6.77 eV, is not enhanced but seems to follow the abundance of Ni. This may be due to efficient condensation of Cr^+ into (Fe,Ni)Si grains as opposed to chemical reactions of Sc and Ti with N and C.

4 CONCLUSIONS

We have studied the Mn II spectra of the Strontium Filament in η Carinae. To this end we computed radiative and electron impact excitation rates for the ion and constructed an appropriate spectral model. This spectral model was used to diagnose the physical conditions of the emitting region. Results are consistent with previous determinations using Sr II, [Sr II], [Ti II] and [Ni II] lines (i.e. $N_e \approx 10^7 \text{ cm}^{-3}$, $T_e \approx 7000 \text{ K}$, and a dilution factor between 10^{-10} and 10^{-9}).

We find the abundance of Mn relative to Ni in gas phase to be roughly consistent with the solar abundance ratio, a result that is similar to that of Cr but unlike the overabundances of Ti and Sc.

These unusual gas-phase abundances in the strontium filament probably arise from a selective chemical fractionation process between the gas and condensates. In the C and O poor, and N-rich gas of the ejecta, Ti condenses as TiC at high temperatures, followed by (Fe,Ni)-silicide at lower temperatures. Scandium enters TiC in solid solution as ScN and Cr alloys with the (Fe,Ni)-silicide. The condensation sequence of these elements is similar to that expected

in a solar-composition gas except that here, very different minerals form early in the depleted C, O enriched N gas.

The most refractory elements, Ti and Sc, should condense in the high-temperature regions closest to the central star, whereas Fe, Ni and Cr should condense at larger distances in cooler ejecta. Condensation in equilibrium should remove Sc and Ti from the gas before Ni and Cr, which would decrease the Sc/Ni and Ti/Ni in gaseous state. This is opposite to what is observed.

An scenario of relative enrichment of Ti and Sc in the gas is by selective destruction of Ti- and Sc-bearing dust. This would involve a three-step process. First, refractory TiC condenses with ScN in solid solution. Secondly, the dust and gas are separated in the expanding ejecta. The gas opacities in the expanding ejecta may drop, allowing radiation-driven evaporation of dust. This leads to the third step, the evaporation of the refractory Ti- and Sc-bearing dust, which is the dust closest to the central source and most exposed to radiation. This three-step process, promises to explain the high Sc/Ni and Ti/Ni ratios observed in the gas and is testable by additional quantitative analysis of other elements (e.g. Al, Ca) with different volatilities which also condense into phases other than refractory carbides and silicides.

The other scenario could be non-equilibrium condensation of Fe-peak elements due to the fact that the elements with the lowest first ionization potential tend to remain photoionized and cannot condense as efficiently as other elements in their neutral state.

ACKNOWLEDGMENTS

MAB acknowledges financial support from grants from the NASA Astronomy and Physics Research and Analysis Programme (award NNX09AB99G) and the Space Telescope Science Institute (project GO-11745). HH acknowledge support from the Swedish Research Council (VR). Based on observations made with the NASA/ESA *Hubble Space Telescope*, obtained (from the Data Archive) at the Space Telescope Science Institute, which is operated by the Association of Universities for Research in Astronomy, Inc., under NASA contract NAS 5-26555. These observations are associated with programmes 8036, 8327, 8483, 8619 and 9420. Work by KL was supported by the National Science Foundation grant AST 0807356 and while working at the Foundation.

REFERENCES

- Badnell N. R., 1986, *J. Phys. B: Atomic Molecular Phys.*, 19, 3827
- Bautista M. A., Peng J., Pradhan A. K., 1996, *ApJ*, 460, 372
- Bautista M. A., Gull T. R., Ishibashi K., Hartman H., Davidson K., 2002, *MNRAS*, 331, 875
- Bautista M. A., Hartman H., Gull T. R., Smith N., Lidders K., 2006, *MNRAS*, 370, 1991
- Bautista M. A., Ballance C., Gull T. R., Hartman H., Lidders K., Martínez M., Meléndez M., 2009, *MNRAS*, 393, 1503
- Berrington K. A., Burke P. G., Eissner W., Norrington P. N., 1995, *Comput. Phys. Communications*, 92, 290
- Burgess A., 1974, *J. Phys. B: Atomic Molecular Phys.*, 7, L364
- Cardelli J. A., Clayton G. C., Mathis J. S., 1989, *ApJ*, 345, 245
- Davidson K., Humphreys R. M., 1997, *ARA&A*, 35, 1
- Davidson K., Dufour R. J., Walborn N. R., Gull T. R., 1986, *ApJ*, 305, 867
- Davidson K., Ebbets D., Weigelt G., Humphreys R. M., Hajian A. R., Walborn N. R., Rosa M., 1995, *AJ*, 109, 1784
- Dufour R. J., Glover T. W., Hester J. J., Currie D. G., van Orsow D., Walter D. K., 1997, in Nota A., Lamers H. J. G. L. M., eds, *ASP Conf Ser. Vol. 120, Luminous Blue Variables: Massive Stars in Transition*. Astron. Soc. Pac., San Francisco, p. 255
- Ebbets D. C., Walborn N. R., Parker J. Wm., 1997, *ApJ*, 489, L161

- Eissner W., Nussbaumer H., 1969, *J. Phys. B: Atomic Molecular Phys.*, 2, 1028
- Gomez H. L., Vlahakis C., Stretch C. M., Dunne L., Eales S. A., Beelen A., Gomez E. L., Edmunds M. G., 2010, *MNRAS*, 401, 48
- Hamann F., Davidson K., Ishibashi K., Gull T. R., 1999, in Morse J. A., Humphreys R. M., Damineli A., eds, *ASP Conf. Ser. Vol. 179, Eta Carinae at the Millenium*. Astron. Soc. Pac., San Fransisco, p. 119
- Hartman H., Gull T., Johansson S., Smith N. (HST Eta Carinae Tresury Project Team Collaboration), 2004, *A&A*, 419, 215
- Hillier D. J., Davidson K., Ishibashi K., Gull T., 2001, *ApJ*, 553, 873
- Hillier D. J. et al., 2006, *ApJ*, 642, 1098
- Hummer D. G., Berrington K. A., Eissner W., Pradhan A. K., Saraph H. E., Tully J. A., 1993, *A&A*, 279, 298
- Irvine W. M., Knacke R. F., 1989, *Origin and Evolution of Planetary and Satellite Atmospheres*. University of Arizona Press, Arizona
- Ishibashi K. et al., 2003, *AJ*, 125, 3222
- Kling R., Schnabel R., Griesmann U., 2001, *ApJS* 134, 173
- Kurucz R., Bell B., 1995, Data base at <http://www.pmp.uni-hannover.de/cgi-bin/ssi/test/kurucz/sekur.html>
- Lodders K., 2003, *ApJ*, 591, 1220
- Lodders K., Palme H., Wlotzka F., 1993, *Meteoritics*, 28, 538
- Lucy L. B., 1995, *A&A*, 294, 555
- Martinson I., Curtis L. J., Brzozowski J., Buchta R., 1973, *Phys. Scr.*, 8, 62
- Meynet G., Maeder A., 2002, *ASPC*, 274, 17
- Pinnington E. H., Lutz H. O., 1974, *Canadian J. Phys.*, 52, 1253
- Pinnington E. H., Guo G., Ji Q., Berends R. W., Ansbacher W., Biemont E., 1992, *J. Phys. B: Atomic Molecular Optical Phys.* 25, 475
- Ralchenko Yu., Jou F.-C., Kelleher D. E., Kramida A. E., Musgrove A., Reader J., Wiese W. L., Olsen K., 2008, *NIST Atomic Spectra Database* (version 3.1.2) (online), available at <http://physics.nist.gov/asd3> (2008 April). NIST, Gaithersburg, MD
- Smith N., Brooks K. J., Koribalski B. S., Bally J., 2006, *ApJ*, 645, L41
- Tapia M., Roth M., Vazquez R. A., Feinstein A., 2003, *MNRAS*, 339, 44
- Thé P. S., Graafland F., 1995, *Rev. Mexicana Astron. Astrofisica. Ser. Conf.*, 2, 75
- Verner K., Gull T. R., Bruhweiler F., Johansson S., Ishibashi K., Davidson K., 2002, *ApJ*, 581, 1154
- Verner K., Bruhweiler F., Gull T., 2005, *ApJ*, 624, 973
- Zethson T., Gull T. R., Hartman H., Johansson S., Davidson K., Ishibashi K., 2001, *AJ*, 122, 322

This paper has been typeset from a \LaTeX file prepared by the author.